Ultrahigh Throughput Silicon Nanomanufacturing by Simultaneous Reactive Ion Synthesis and Etching

Yi Chen, Zhida Xu, Manas R. Gartia, Daren Whitlock, Yaguang Lian, and G. Logan Liu*

Micro and Nanotechnology Laboratory, Department of Electrical and Computer Engineering, University of Illinois at Urbana—Champaign, Urbana, Illinois 61801, United States

ABSTRACT One-dimensional nanostructures, such as nanowhisker, nanorod, nanowire, nanopillar, nanocone, nanotip, nanoneedle, have attracted significant attentions in the past decades owing to their numerous applications in electronics, photonics, energy conversion and storage, and interfacing with biomolecules and living cells. The manufacturing of nanostructured devices relies on either bottom-up approaches such as synthesis or growth process or top-down approaches such as lithography or etching process. Here we report a unique, synchronized, and simultaneous top-down and bottom-up nanofabrication approach called simultaneous plasma enhanced reactive ion synthesis and etching (SPERISE). For the first time the atomic addition and subtraction of nanomaterials are concurrently observed and precisely controlled in a single-step process permitting ultrahigh-throughput, lithography-less, wafer-scale, and room-temperature nanomanufacturing. Rapid low-cost manufacturing of high-density, high-uniformity, light-trapping nanocone arrays was demonstrated on single crystalline and polycrystalline silicon wafers, as well as amorphous silicon thin films. The proposed nanofabrication mechanisms also provide a general guideline to designing new SPERISE methods for other solid-state materials besides silicon.

KEYWORDS: simultaneous plasma-enhanced reactive ion synthesis and etching (SPERISE) · synchronized bottom-up and top-down nanomanufacturing · nanomushroom · plasma-assisted nucleation · inward penetrated ion oxidation

The long-term industrial and societal impact of semiconductor nanofabrication technology depends on its production rate, reliability, robustness, yield, cost, and the integration capability with micro- and macroscale systems. In recent years, various nanofabrication technologies have been developed for creating one-dimensional nanostructures on semiconductor substrates, including periodical or random 3D nanowires,[1] nanopillars,[2] and nanocone arrays.[3]

Previously these semiconductor nanostructures were created by either bottom-up or top-down processes. Bottom-up processes refer to growth techniques based on various phase transition mechanisms, such as vapor—solid (VS),[4] vapor—liquid—solid (VLS),[5] and solid—liquid—solid (SLS).[6] Top-down processes rely on nanoscale patterning with various nanolithography techniques, such as photo-, electron beam, nanosphere,[3] nanoimprint,[7] soft,[8] and block copolymer lithography,[9] followed by an anisotropic plasma etching or metal templating followed by metal-assisted chemical etching.[10] All of these approaches involve nanoscale prepatterning, surface-area-sensitive assembly processes or extreme fabrication conditions; therefore, they are often limited by the associated high cost and low yield as well as the consequent industry incompatibility.

By presenting the SPERISE technology as a semiconductor nanomanufacturing process, we demonstrate an integrated nanoscale bottom-up synthetic and top-down etching approach with ultrahigh throughput, reliability, and high yield at relatively low costs. The SPERISE approach has immediate scientific and industrial applications.

RESULTS

Nanofabrication Process and Mechanism. The key mechanism underlying the SPERISE method is the concurrent reactive ion nucleation process with the reactive ion etching process. In a plasma-enhanced multiple ion reaction system, the nanoscale gas-to-solid phase transition synchronizes with the nanoscale solid-to-gas phase transition, which results in pseudo-uniform, complex, oxide nanoparticle arrays gradually grown over the entire surface of silicon wafers. These arrays act as the etch mask for the simultaneous anisotropic silicon etching. The SPERISE nanofabrication process is shown in Figure 1a. Bare silicon substrates are prepared with a standard process (see Methods) and cleaned with a wet etching process to remove the native oxide layer on the surface. In a reactive ion etcher chamber, a silicon nanocone array is

* Address correspondence to loganliu@illinois.edu.

Received for review July 4, 2011 and accepted September 21, 2011.

Published online September 21, 2011
10.1021/nn2024754

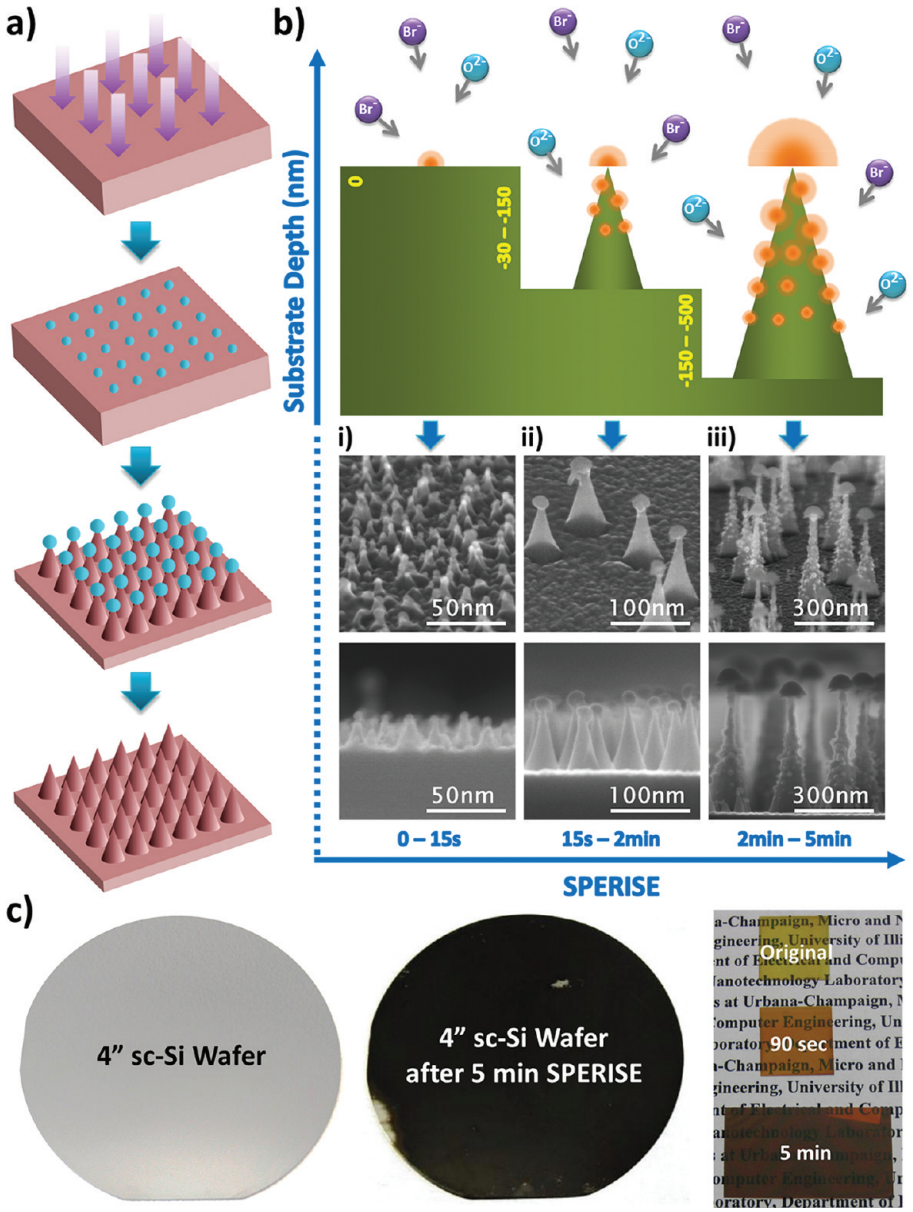

Figure 1. Simultaneous plasma enhanced reactive ion synthesis and etching (SPERISE) process and Si nanocone formation mechanism. (a) Process flow of the novel simultaneous bottom-up and top-down nanomanufacturing process. Pseudo-randomly distributed silicon oxybromide nanodots were synthesized on the planar silicon substrate surface in the first few seconds of the SPERISE process with the mixtures of oxygen and bromine plasma. The oxide nanodots grew to hemispheres by a phase-transition nucleation process, and they acted as a protective nanomask for the simultaneous reactive ion etching of the underneath silicon structures. Depending on the growth rate of the oxide hemispheres and the crystalline structures of the silicon substrates, nanocones with different aspect ratios will be formed. The silicon oxybromide nanohemispheres on top of nanocones can be removed by wet oxide etchant. (b) Detailed schematic drawing of the three typical stages in the SPERISE process. Bromine and oxygen reactive ions interact with silicon to form synthesized oxide hemisphere and dots (orange) and etched silicon cone structure (green). Both illustration and corresponding SEM images at (i) 0–15 s, (ii) 15 s–2 min, and (iii) 2–5 min in the SPERISE process manifest this unique nanomanufacturing method. (c) Wafer-level SPERISE nanomanufacturing. The SPERISE process creates very high density and high aspect ratio nanocone arrays uniformly on the whole surface of a 4″ single crystalline Si (sc-Si) wafer, and thus turns it from shining and reflective (left image) to complete black or light absorbing (middle image). The SPERISE process also applies for amorphous silicon thin film and creates uniform nanostructures on the surface (right image).

formed on the entire substrate surface *via* the single-step SPERISE process with a reactive ion mixture of hydrogen bromide (HBr) and oxygen (O_2) (see Methods). Bromine ions are the primary etching plasma to react with silicon atoms from the top surface layer gradually to inside layers, while oxygen ions, bromine ions, and silicon ions combined together comprise the building blocks to synthesize the complex silicon oxybromide compound on top of the substrate surface layer. The simultaneous bottom-up and top-down reactions can be summarized in several chemical reaction formulas (eq 1) by including

the silicon oxidation.

$$\begin{aligned} Si + 4Br^- &\xrightarrow{\text{etching}} SiBr_4 \\ SiBr_4 + O^* &\xrightarrow{\text{synthesis}} SiBr_xO_y \\ Si + 2O^* &\xrightarrow{\text{oxidation}} SiO_2 \end{aligned} \quad (1)$$

Initially, randomly distributed seed points will be nucleated when bromine ions and oxygen ions simultaneously meet at some exposed silicon crystal lattice points on the surface (Figure 1b,i).[11] Within several seconds, the seed points will quickly grow into nanodots through a gas-to-solid nucleation process. These nanodots are less than 10 nm in diameter indicated by the corresponding scanning electron microscopy (SEM) images (Figure 1b,i). What occurs at this stage is primarily a bottom-up process, creating the protective nanoscale mask array for both the subsequent nucleation and etching processes. The nanodots will keep growing over time around the initial nucleation point into larger hemispherical nanoparticles (Figure 1b,ii). Simultaneously with the above nucleation process, the exposed silicon surface is continuously etched by bromine ions. Because HBr has a very high reaction selectivity of silicon to silicon oxide (200:1), the growing silicon oxybromide ($SiBr_xO_y$) nanoparticle array acts as a constantly growing etch mask that protects the covered silicon surface. Consequently, the longitudinal nanostructures will be created by this self-controlled anisotropic etching process. As shown in the SEM image (Figure 1b,ii), the bottom structures are nanocones with smooth sidewalls and the top structures are nanohemispheres. The nanodots eventually grow into nanohemispheres because the reactive ion flux is highly directionally from the top, so the nucleation will preferably happen on the top of the nanodots. A similar nanoscale process was observed before;[12] however, the mechanisms controlling this process were not explored. As the etching of the nanocones continues, oxide nucleation nanodots are also formed on the sidewall of newly exposed silicon nanocone surface besides the further growth of the nanohemispheres on the top of the nanocones (see Figure 1b,iii). A nanomushroom structure can be seen with the sidewall covered by a layer of oxide nanodots (SEM image in Figure 1b,iii). The SEM image also shows that the size and density of the nanodots synthesized on the sidewall gradually decrease from the top to the bottom part of the nanocones and there are no nanodots on the bottom of the sidewall at all. The size difference of the sidewall nanodots at different heights directly reflects the different time spent in the localized reactive ion synthesis process. This observation strongly supports the plasma enhanced oxide nanodots nucleation mechanism.

The density of the initially synthesized nanodots determines the density of the final silicon nanocone array, hence the density of the nanocone array is controllable by varying the HBr and O_2 plasma concentrations (see Supporting Information, Figure 1). The average height of the nanocones can be controlled by varying the time of the SPERISE process (see Supporting Information, Figure 2). The SPERISE method can be implemented with a standard reactive ion etcher and requires neither prepatterning in conventional top-down etching methods nor noble metal catalyst in conventional bottom-up synthesis methods. Moreover, the SPERISE fabrication process is capable of a variety of substrate sizes, including full wafer fabrication in the same high throughput fashion. It is also independent of crystallographic orientation, and works for single crystalline or monocrystalline (sc-Si), polycrystalline (pc-Si), and amorphous (a-Si) silicon wafers and thin films. As shown in Figure 1c, a 4″ sc-Si wafer and an a-Si thin film on a glass substrate with very high density and uniformity nanocone arrays on the entire surface were successfully fabricated by a 5-min SPERISE process. By properly choosing reactive ion species, SPERISE process of III–V semiconductor nanomaterial may also be supported by the same mechanism, which is under investigation.

The Crystallographic Dependence of the SPERISE Reaction and the Underlying Mechanisms. In the scanning electron microscopy study, we found the nanostructures created on the three kinds of substrates after the same SPERISE process are quite different, which are nanocones, nanopillars, and nanofrustums for the monocrystalline (Figure 2a,d,g,j), polycrystalline (Figure 2b,e,h,k), and amorphous (Figure 2c,f,i,l) silicon substrates, respectively. The monocrystalline nanocones (Figure 2a,d) have very sharp tips covered by oxide nanohemispheres; the polycrystalline nanopillars (Figure 2b,e) are high aspect ratio structures with identical top and base diameters; and the amorphous nanofrustums (Figure 2c,f) are low aspect ratio structures with a base diameter slightly larger than the top diameter. However, after the oxide removal, all three nanostructures became nanocones with sharp tips and smooth surface profiles (Figure 2g,h,i), which indicates that the polycrystalline nanopillars and the amorphous nanorods have a relatively thick layer of oxide covered on the surface of the sidewalls. In addition, there is a noticeable height reduction from the original nanopillars/nanorods to the nanocones after oxide removal, which is primarily due to the removal of the nanohemispheres on the top of the nanocones. In the cross-sectional views of the three nanocones (Figure 2j,k,l), the height, base diameter, and the aspect ratio differences exhibit more clearly. These differences are consistently observed in all of our experiments. We believe that the geometric differences of the nanostructures based on the three different crystallographic substrates imply an inherent mechanism in the SPERISE process. It is crucial to explore this mechanism for

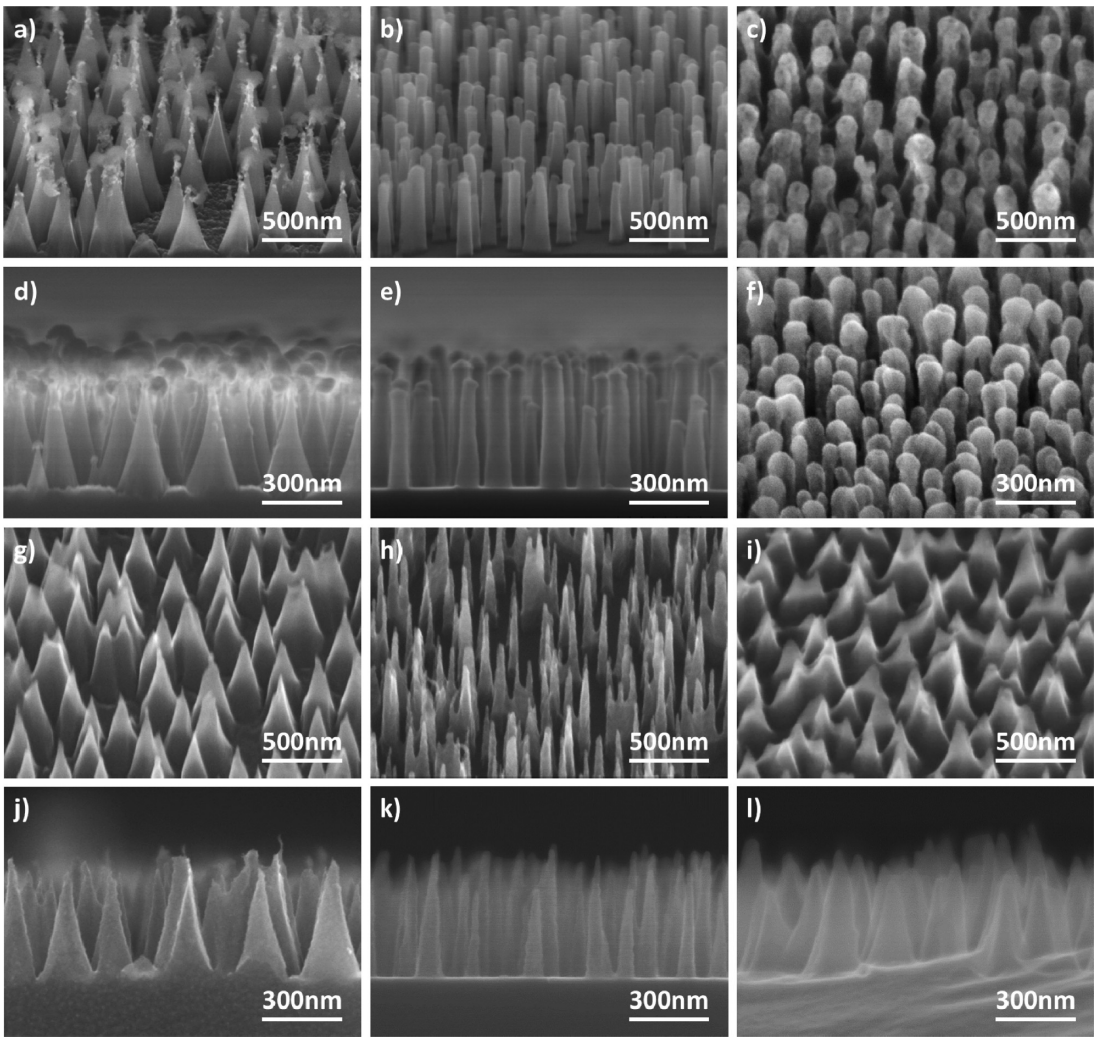

Figure 2. SEM images of nanostructures created by SPERISE process. (a−f) Nanostructure profiles on (a,d) single crystalline, (b,e) polycrystalline, and (c,f) amorphous silicon substrates before oxide removal. Nanocones, nanopillars, and nanorods are created on these three substrates, respectively, with clearly visible oxide nanohemispheres on top. (g−l), Nanostructure profiles on (g,j) single crystalline, (h,k) polycrystalline, and (i,l) amorphous silicon substrates after oxide removal. All three substrates become nanocones with extremely smooth sidewall and sharp tips. The nanocones showed different aspect ratios, with the sharpest nanocones on polycrystalline substrate and the most obtuse nanocones on amorphous substrate, which suggests the crystalline structures of the substrates impacts the nanocone profiles.

better understanding as a guideline for controllable and deterministic nanofabrication.

In an effort to understand this mechanism as a guideline for controllable and deterministic nanofabrication, we carried out a systematic morphological measurement and comparative analysis of the nanostructures for three kinds of silicon substrates under a typical nanofabrication condition. All results are plotted in Figure 3d−i and the information about the nanostructures morphology measurements, calculations, and model fittings is in Methods. Figure 3d shows the average heights of nanostructures before (solid lines) and after (dashed lines) the oxide removal. All these data indicate that the height, h, of the nanostructures before and after oxide removal maintains the relationship $h_{sc\text{-}Si} < h_{pc\text{-}Si} < h_{a\text{-}Si}$, and the total height reduction (dash−dot lines) is also in an order $h_{sc\text{-}Si} < h_{pc\text{-}Si} < h_{a\text{-}Si}$. As the height reduction is primarily due to the removal of the synthesized nanohemispheres on top of nanocones, this result implicates the nucleation rate of sc-Si < pc-Si < a-Si, which is consistent with the measured diameter of synthesized nanohemispheres in Figure 3e. As can be seen from the plots, a nanohemisphere of a-Si material grows much faster than those of pc-Si and sc-Si, and a nanohemisphere of pc-Si grows slightly faster than that of sc-Si. Also, we found that the height difference before and after oxide removal (dash−dot lines in Figure 3d) is much larger than the radius of the nanohemisphere. This discrepancy is consistently observed in all experiments; hence it cannot be explained as an error in the measurements. It implicates a unique inherent mechanism in the SPERISE process. The height discrepancy is calculated in Figure 3g, in which a nonlinear

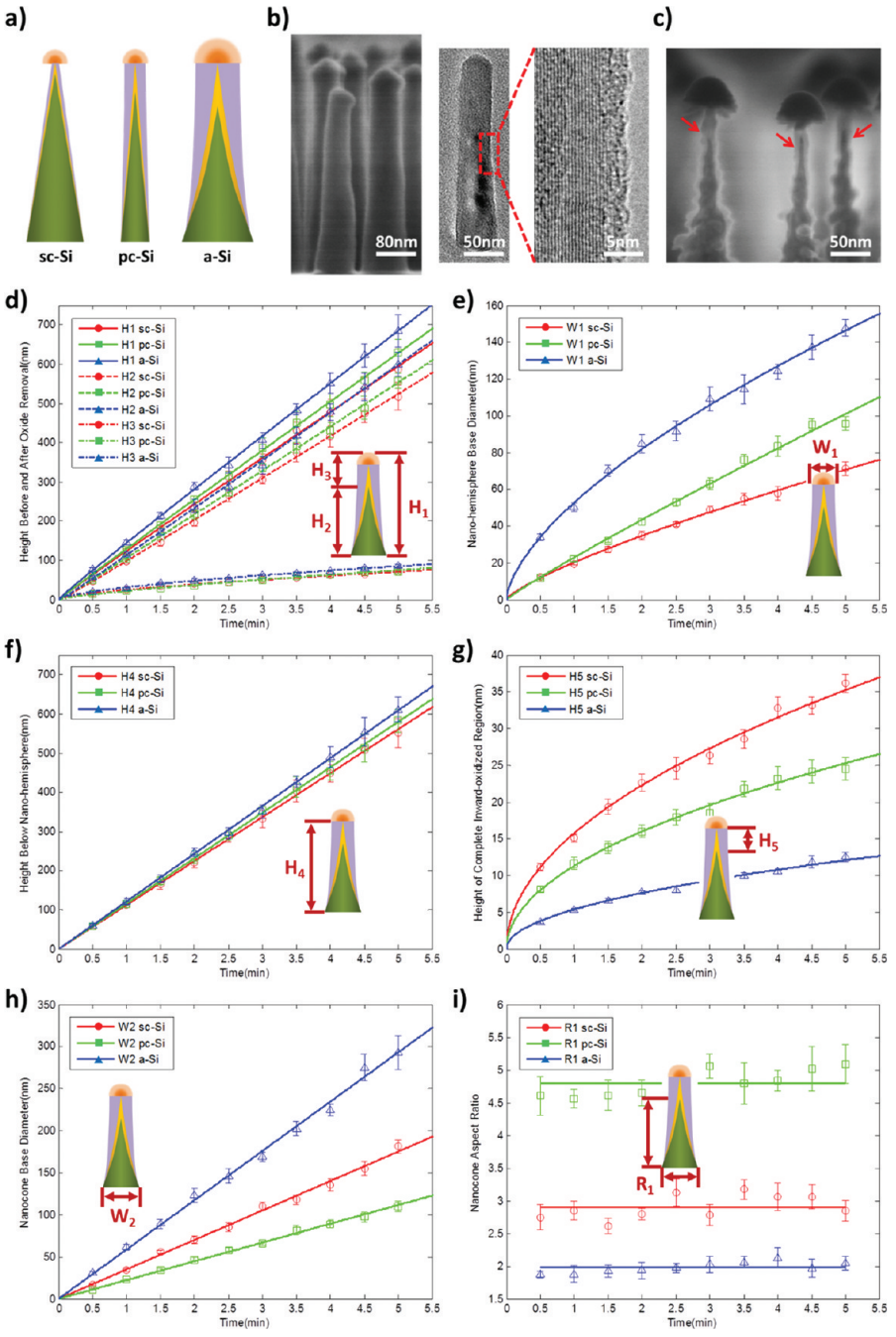

Figure 3. Nanocone profile formation mechanism and characterization for single crystalline (sc-Si), polycrystalline (pc-Si), and amorphous (a-Si) substrates. (a) Schematic of nanostructure profile formation mechanism. The orange half-circle on top represents the synthesized oxide nanohemispheres. The purple, gold, and olive green regions represent the oxide layer created by outward reactive ion nucleation, the oxide layer created by inward penetrated ion oxidation, and the actual nanocone profiles after oxide removal, respectively. (b) TEM image shows core–shell structure of pc-Si nanopillar before oxide removal. The core is the silicon nanocone, and the shell is the oxide layer formed primarily by outward reactive ion nucleation. (c) High resolution SEM image showing the neck region of sc-Si "nanomushrooms". A core–shell structure under the oxide nanohemisphere cap indicates the complete oxidation of the original silicon nanotip, which is primarily caused by inward penetrated ion oxidation. (d) Average height measurements of the nanostructures on sc-Si, pc-Si, and a-Si before and after the oxide removal, as well as total height reduction caused by oxide removal. (e) Average diameter of the oxide nanohemisphere. (f) Average nanocone height below nanohemisphere cap. (g) Average height of complete inward-oxidized region. (h) Average nanocone base diameter. (i) Aspect ratio calculated from the measured average height and base diameter after oxide removal. The inset images represent the corresponding geometries of the plotted data. From d–i, the best fit curves of each data group are also plotted (for models of the curve fitting refer to Methods).

monotonic increase is shown. Furthermore, the base diameter is measured in Figure 2h, in which it increased linearly with rates 35.03 nm/min, 22.32 nm/min, and 58.60 nm/min for sc-Si, pc-Si, and a-Si, respectively. The aspect ratio is plotted in Figure 2i by dividing the measured height after oxide removal by the

base diameter. It is very consistent with different processing times, with around 3:1, 5:1, and 2:1 for sc-Si, pc-Si, a-Si nanocones, respectively. These data demonstrate the high repeatability and controllability of the SPERISE process.

On the basis of the above findings, we propose that the sidewall oxide formation was concurrently governed by two different physical and chemical processes (Figure 3a). One process is the bromine and oxygen ion associated nucleation on the newly etched silicon surface, which shares the same mechanism with the nanohemisphere synthesis (purple region in Figure 3a). The other process is the inward oxidation in which the oxygen and bromine ions penetrate the nucleated oxide layer and associate with the sidewall silicon crystal lattices to form oxide inward from the original etched sidewall (yellow region in Figure 3a).

In the first process, the oxide layer grows outward from the original sidewall. The rate of the nucleation process for both sidewall oxide layer and nanohemisphere is directly related to the etch rate of silicon materials because quicker etching produces higher localized silicon ion concentration near the silicon nanocones surface, hence the possibility of nucleation events is increased. As shown by the solid lines in Figure 3f, the etch rate of the three types of silicon materials is in the order of sc-Si < pc-Si < a-Si, with 112.2, 115.9, and 121.7 nm/min for sc-Si, pc-Si, a-Si nanocones, respectively. Consequently, the growth of the diameter of nanohemispheres (Figure 3e) is also in the same order. Furthermore, the sidewall profile differences between the sc-Si nanocones, pc-Si nanopillars, and a-Si nanorods shown in Figure 2a,b,c, can be also explained with this mechanism, by which the sidewall oxide thickness maintains the same order as the etch rate (sc-Si < pc-Si < a-Si). Meanwhile, the sidewall profile is also determined by the difficulties of the reactive ions associating with the sidewall surfaces. The outward nucleation process occurs once the new sidewall silicon surface is exposed. For sc-Si, the reactive ions are preferably associated with exposed and less stable crystal lattice points; therefore, nucleation only occurs at pseudorandom locations and form oxide spots on the sidewalls at low rates (see Figure 1b-iii, Figure 2a,d, and Figure 3c). Only a thin layer of oxide is formed on the sidewalls and the overall structure profile remains nanocones for sc-Si. For pc-Si, the reactive ions are preferably associated with exposed grain boundaries[13] as well as the exposed crystal lattice points on each crystalline patch, hence the nucleation process happens nearly everywhere on the sidewall and a nearly uniform oxide layer forms on the sidewall at higher nucleation rates (see Figure 2b,e and Figure 3b). The nucleation time difference causes a thicker and thinner oxide layer at the top and bottom, respectively; consequently, the overall profile looks like nanopillars for pc-Si. In the case of a-Si, ion association happens everywhere on the sidewall. The nucleation rate is the highest, so a much thicker and uniform oxide layer was formed (see Figure 2c,f) and the top oxide nanohemispheres for a-Si samples are much larger than those for sc-Si and pc-Si samples (see Figure 2a, b,c). The hemispherical caps with protruded rims on the pc-Si nanopillar in the SEM image of Figure 3b clearly separates the bottom-up synthesized structure and top-on etched structure, which supports the plasma assisted nucleation mechanism.

The second process is similar to the thermal oxidation, in which the oxidation happens by inward movement of oxidants rather than by outward movement of silicon.[14] The difference, however, is that in thermal oxidation, the oxidant moves by diffusion along the molecular density gradient. In this process, the oxidant moves by physical bombardment. The thickness of the inward oxidation layer is determined by the thickness of the outward nucleation layer, as the thicker the outward nucleation layer is the harder the ions penetrate it. As shown in Figure 3g, the thickness is sc-Si > pc-Si > a-Si, which is in the reversed order of the nucleation process in Figure 3e. Although the thickness of this oxide layer is minor compared with the outward nucleated oxide, this physical process is critical in explaining the discrepancy of the total height reduction by oxide removal (dash−dot lines in Figure 3d) and the radius of the nanohemisphere (Figure 3e). The core−shell structure with crystalline core and amorphous shell visualized on the sidewall of the nanopillar from the high resolution TEM image of Figure 3b supports the aforementioned outward nucleation and inward oxidation mechanisms. Clear core−shell structures with darker silicon crystal core and brighter oxide shell are also observed near the neck region of the sc-Si nanomushroom shown in Figure 3c. There is a pure oxide region (brighter) between the silicon nanotip (darker) and the oxide nanomushroom cap, which indicates that the region just beneath the mushroom cap has been completely oxidized in the inward oxidation process.

Besides the morphological determination by the aforementioned two processes, because the nanohemispheres act as the etching mask of the silicon, the aspect ratio of the originally etched nanocone profile is determined by the lateral growth rate of the oxide nanohemispheres. The etch directionality is also influenced by the crystallographic orientation of the substrates to some extent due to higher etch rate along the ⟨100⟩ plane than the ⟨111⟩ plane.

Although these nanostructure geometry characterization data vary when changing the fabrication conditions, the mechanisms disclosed here are invariant. The information acquired from this investigation of the underlying physical mechanisms in the novel SPERISE process helps us understand the process and provides

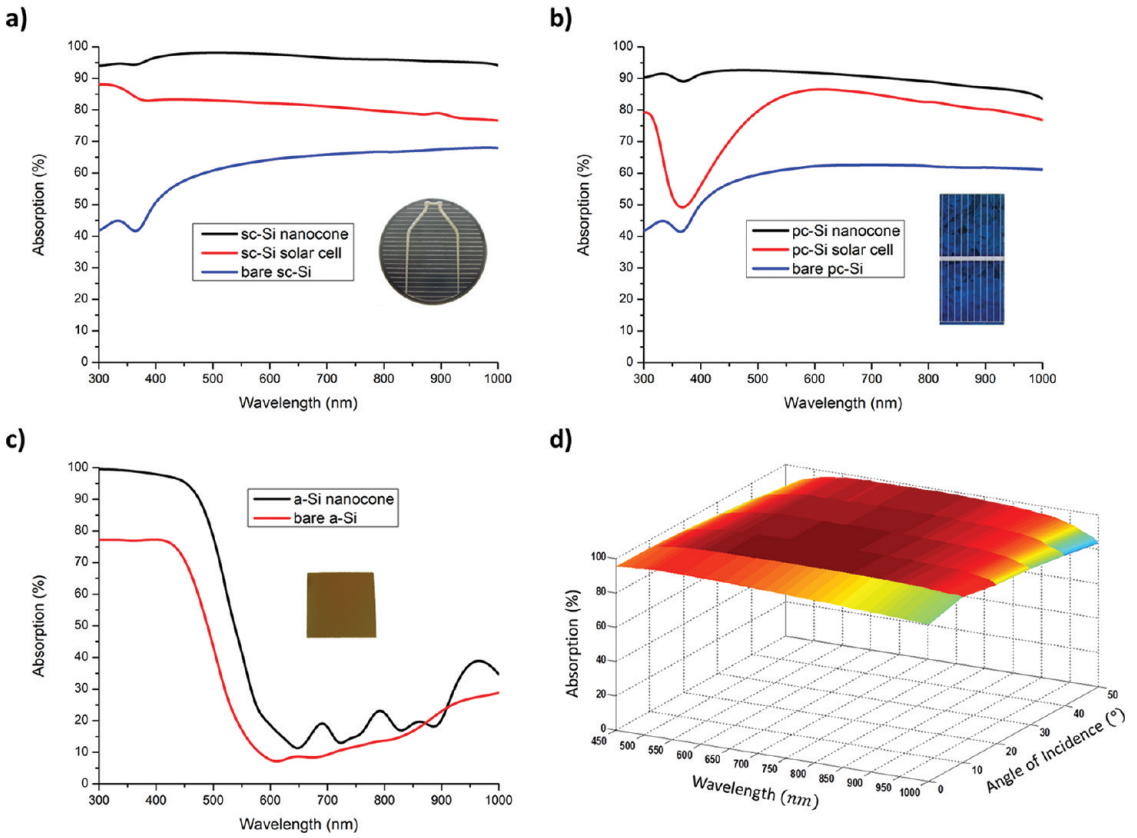

Figure 4. Measured optical absorption of the nanocone array created on different crystalline silicon substrates. (a) The optical absorption of a single crystalline silicon nanocone array substrate in comparison with a bare single crystalline silicon substrate and a commercial single crystalline silicon solar cell with conventional texturing and antireflective coating. The inset graph is the image of the commercial solar cell in our measurement. (b) The optical absorption of a polycrystalline silicon nanocone array substrate in comparison with a bare polycrystalline silicon substrate and a commercial polycrystalline silicon solar cell with conventional texturing and antireflective coating. The inset graph is the image of the commercial solar cell in our measurement. (c) The absorption of an amorphous silicon nanocone array thin film in comparison with a bare amorphous silicon thin film. The inset graph is the image of the amorphous silicon thin film on a glass slide. All absorption spectra in panels a, b, and c were measured under the normal incident light condition. (d) Angle independent absorption of the single crystalline silicon nanocone array. The measurements were done with the incident light from 0°−50°.

guiding principles for controlling and manipulating the nanostructures in industrial manufacturing.

Light Trapping Properties of the Nanocone Array. Here, we demonstrate the light trapping effect of the silicon nanocone wafers produced by the SPERISE as an initial exemplary application in high performance optoelectronics. In fact, the conic structure array is known for impedance matching between two dielectric media by creating the graded permittivity or refractive index layer. Similar conic structures can also be found in the anechoic chamber for radio frequency (RF) electromagnetic waves to completely absorb RF waves.[15]

Compared to the highly reflective surface of the bare sc-Si wafer, the visual appearance of the post-SPERISE processed sc-Si wafer surface appears dark, which indicates a significant reduction in reflectance in the visible spectrum (see Figure 1c, left). The a-Si thin film substrate also becomes darker for longer SPERISE processing times, which indicates the reduction of reflectance in the visible light range (see Figure 1c, right). Figure 4 shows the measured optical absorption of the wafer-scale sc-Si, pc-Si, and a-Si substrates, as well as corresponding commercial c-Si solar cells and bare a-Si substrates from all incident angles at wavelengths ranging from 300 to 1000 nm (see Methods). Remarkably, the sc-Si nanocone samples produced by the SPERISE process have more than 90% absorption in the ultraviolet (UV), visible, and near-infrared (NIR) light ranges (Figure 4a) without any additional antireflective coating, and have better absorption than not only the bare silicon (50%-60%) and commercial sc-Si solar cells (<80%) but also other reported silicon nanostructures.[1,3,16] Compared with bare pc-Si substrates and commercial pc-Si solar cells with conventional antireflective coatings, the enhanced absorption of the pc-Si nanocone substrate is even more pronounced as shown in Figure 4b. The conventional antireflection coatings are ineffective (<60%) in the blue light region as indicated by its reflective color. In sharp contrast, the pc-Si nanocone substrate has higher than 90% absorption in the whole visible light region and only drops slightly below 90% in the NIR region. Compared with

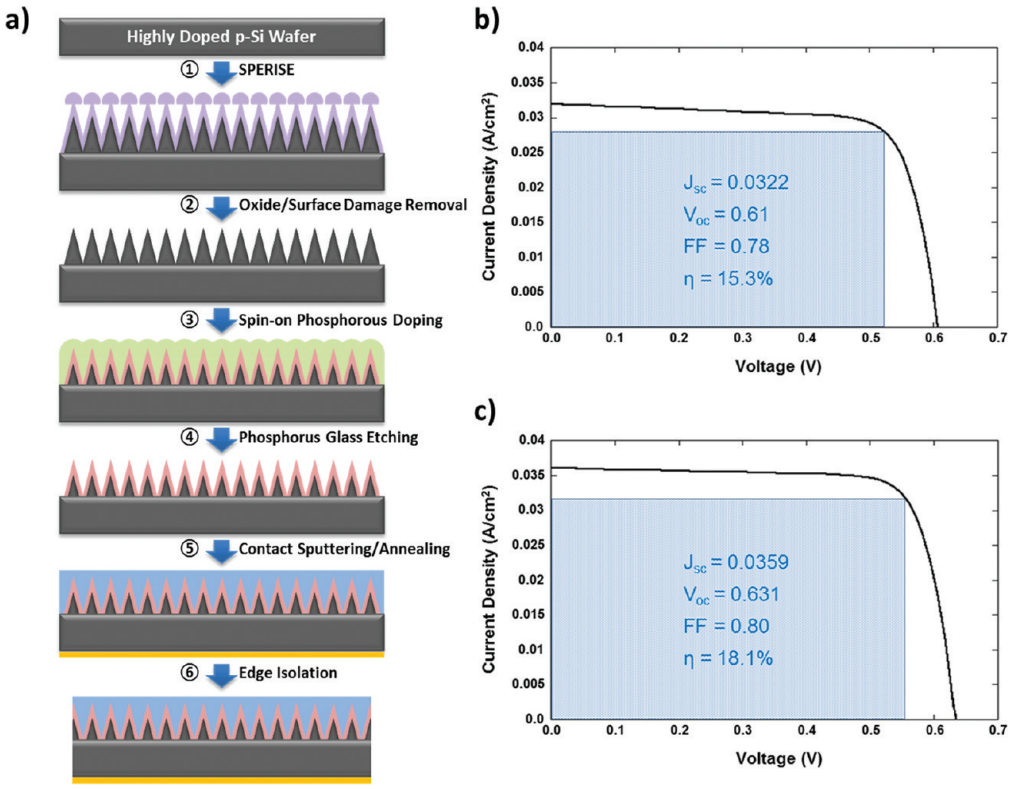

Figure 5. Nanocone array solar cell fabrication process and *I*−*V* characteristics. (a) Schemic nanocone array solar cell fabrication process. A nanomushroom array was first created on a planar surface by the SPERISE process, followed by the oxide removal and surface damage removal. Afterward, a spin-on phosphorus doping was performed followed by a phosphorus glass etching to form a p−n junction. Then, a layer of ITO and Au were sputtered and then annealed to form conformal top and bottom contacts, respectively. At last, edge isolation was completed by mechanical sawing. The planar control solar cell was fabricated with steps 3−6. (b) *I*−*V* characteristics of planar control solar cell, which had J_{sc} = 33.2 mA/cm^2, V_{oc} = 610 mV, fill factor = 0.78, and efficiency = 15.3%. (c) *I*−*V* characteristics of nanocone array solar cell, which had J_{sc} = 35.9 mA/cm^2, V_{oc} = 631 mV, fill factor = 0.80, and efficiency = 18.1%.

the uniform, thin film a-Si deposited on glass, the absorption enhancement of the a-Si nanocone structures in the visible light region is remarkable; the absorption is nearly 100% in the blue and near UV light regions at a-Si bandgap of ~1.7 eV (see Figure 4c). The above demonstrated optical absorption enhancement is also supported by theoretical simulations (see Supporting Information, Figure 3).

The absorption of pc-Si nanocone array is slightly lower than sc-Si nanocone array. We believe it is likely due to the geometrical differences of the nanocones on these two substrates rather than the material property differences. As shown by the SEM images in Figure 2g, h, the diameters of the sc-Si nanocones linearly decrease from the wide base to the sharp, pointy top, resulting in a gradual transition of the effective refractive index,[3] while the pc-Si nanocones are much thinner compared with sc-Si nanocone and have smaller vertical gradients in diameter. Another possible explanation is that pc-Si nanocone arrays with open, flat spaces at the base still allow for weak reflection of light waves incident at the normal angle while the tightly packed sc-Si nanocone array provides better coverage of the substrate surface, thus eliminating the wave reflection at the normal angle and effectively trapping more photons.[17]

As can be seen from a typical absorption spectrum of a sc-Si nanocone substrate reflecting the relationship of absorbance to angle of incidence (AOI) and wavelength (Figure 4d) (see Methods), the absorption of the nanocone substrate is around 99% in the visible light range at all AOI from 0°−50° and slightly drops below 90% beyond 1000 nm. The reason for the angle independence property is probably that the pseudo-random spatial arrangements of tightly packed nanocones eliminated the anisotropic angular absorption inevitably caused by perfect periodic structures.[17] The angle independence makes the nanocone substrates better omnidirectional antireflectors than regular nanoarray substrates.

Nanocone Array Silicon Solar Cell. As shown above, the silicon nanocone arrays created by the SPERISE process have remarkable omnidirectional light absorption enhancement. To demonstrate the photovoltaic application of this nanomanufacuring method, a batch of single p−n junction solar cells was fabricated by the process shown by the schematic Figure 5a. First, a high density nanomushroom array was formed on highly

doped (0.001−0.005 Ω·cm) p-type monocrystalline silicon wafer (University Wafer) by the SPERISE process as discussed before. The substrate then went through the HF oxide removal and HNO3/HF (50:1) surface damage removal processes. The p−n junction was formed by spin-on phosphorus doping processes (P509 Dopant from Filmtronics), and a radial junction with junction depth around 200 nm was formed at 950 °C for 10 min. Phosphorus glass etching is preformed afterward. ITO and Au sputtering followed by a rapid thermal annealing (RTA) at 400 °C led to a conformal front and back contact respectively covering the whole surface. The ITO conformal top contact has two advantages: (i) compared with conventional finger grid top contact, it shortens the travel distance of charge carriers, so that it significantly reduces the series resistance; (ii) it reduces surface recombination by eliminating the dangling bonds on the Si surface. At last, edge isolation is achieved by mechanical sawing. Control planar silicon solar cell was fabricated with the same process from phosphorus doping step-to-edge isolation step. Even though only sc-Si wafer was used in this proof-of-concept study, the fabrication procedure demonstrated here should be transferable to pc-Si wafer and a-Si thin film solar cells.

Figure 5b,c show the $I-V$ characteristics of nanocone black silicon and planar silicon control solar cells under AM 1.5G illumination. The average J_{sc} of planar and nanotextured sc-Si solar cell are 32.2 mA/cm^2 and 35.9 mA/cm^2, respectively. Although the solar-weighted absorption of sc-Si nanocone surface has around 20% enhancement over a planar silicon surface, the J_{sc} of nanotextured sc-Si solar cell has only 11.5% enhancement over a planar sc-Si control cell, which might be due to the larger surface area, and thus heavier surface recombination of nanocone array solar cell. It indicates that surface recombination has a strong impact on the ultimate cell performance; thus, a better surface passivation technique needs to be considered in future work to maximize the light absorption gain by the nanostructures. The V_{oc} for nanocone and planar solar cells are 631 mV and 610 mV, respectively. The enhancement of V_{oc} might be contributed by the more effective charge carrier collection through radial junction. The fill factor of a nanocone solar cell is 0.80, which is slightly higher than 0.78 of a planar solar cell. The efficiency of a nanocone solar cell is 18.1%, which has 18.3% enhancement over the 15.3% of a planar solar cell, and is better than the efficiency of similar nanotextured solar cells reported in the literature.

CONCLUSION

We presented a simultaneous plasma enhanced reactive ion synthesis and etching (SPERISE) technology, and a proposed explanation of the fundamental mechanism underlying this lithography-less, high-throughput, semiconductor nanocone array formation process. It is the first demonstrated simultaneous and synchronized top-down and bottom-up manufacturing method. On the basis of this nanofabrication mechanism, we have applied the one-step wafer-scale nanomanufacturing process for antireflective silicon wafer productions. This wafer-scale fabrication scheme works for all types of sc-Si, pc-Si, and a-Si wafers and even silicon thin film on flexible substrates. We successfully showed that the nanoconic silicon wafers fabricated by SPERISE technology have an extremely high absorption of incident light in a broad wavelength range and at nearly all angles of incidence. Without involving any prepatterning or nanoparticle assembly processes, this new nanomanufacturing method is highly reliable, repeatable, and controllable, as well as extremely time and cost-effective, as nanocone array structures on the entire wafer surface can be faithfully created within a few minutes under room temperature. Considering all the above advantages over current antireflection coating processes, we believe that this technology has an inherent capability to monolithically integrate with standard silicon device fabrications and can be readily adopted by today's silicon solar cell and high performance photonics industries.

METHODS

Substrates Preparation. The silicon substrates used in our experiment are single crystalline, polycrystalline, and amorphous silicon samples. The single crystalline silicon (sc-Si) substrate was a phosphorus doped p+ Si wafer with resistivity 0.001−0.005 Ω·cm and crystalline orientation ⟨100⟩. The polycrystalline silicon (pc-Si) substrate was an n+ polycrystalline silicon thin film of about 1 μm thickness deposited on phosphorus doped p+ Si wafer by a low pressure chemical vapor deposition (LPCVD) process. The amorphous silicon (a-Si) substrate was a thin layer (~1 μm) of a-Si deposited on a microscope slide or cover glass through a plasma-enhanced chemical vapor deposition (PECVD) process.

Nanofabrication Process. Each one of the sc-Si, pc-Si, and a-Si substrates prepared by above processes were chosen, and first cleaned by acetone and isopropyl alcohol, then followed by a hydrogen fluoride (HF) native oxide removal. The precleaned sc-Si, pc-Si, and a-Si substrates were then placed in the PlasmaTherm SLR-770 inductively coupled plasma (ICP) reactive ion etcher (RIE) with preset conditions for a certain time period, depending on the desired aspect ratio and height of nanostructures. All preset conditions will influence the nanostructures in different significance, including the mixture ratio of hydrogen bromide (HBr) and oxygen (O_2), radio frequency of ICP generator, temperature, pressure, and radio frequency of RIE chamber. A postfabrication hydrogen fluoride (HF) wet chemical etching is performed for oxide removal. In our experiments, the typical aspect-ratios are 3:1, 5:1, and 2:1, and etch rates are 112.2, 115.9, and 121.7 nm/min for sc-Si, pc-Si, a-Si substrates, respectively.

Although sharing the similar equipment with other RIE processes, the SPERISE process has clear differences with regular RIE processes. The most important influential factor is the mixture ratio of hydrogen bromide (HBr) and oxygen (O_2), as HBr is the primary etching gas, and O_2 mainly determines the silicon oxybromide synthesis process. If the mixture ratio is too high, the top-down etching process will proceed much faster than the bottom-up synthesis process, in this case the SPERISE process becomes a regular RIE etching. In contrast, if the mixture ratio is too low, the silicon oxybromide synthesis happens too rapidly and quickly prohibits the etching process on the whole surface. Only an appropriate mixture ratio can lead to a steady simultaneous top-down and bottom-up process, and eventually form a high aspect ratio nanocone structure with oxide nanohemisphere on top. The mixture ratio for this equipment is 200:7−200:13 for an active SPERISE process; however, it could vary for other reactive ion etchers.

The radio frequency wave energy of the RIE chamber cannot be too high either, or otherwise the physical bombarding of the plasma ions will damage the top and sidewall of the synthesized oxide protective mask, and then disturb the equilibrium of the simultaneous bottom-up and top-down process.

The SPERISE process is not very sensitive to other conditions, such as temperature, chamber pressure, and the radio frequency of the ICP generator. These conditions primarily influence the density and aspect ratio of the nanocone array structures. The influences of all aforementioned conditions have been verified in our experiments.

Nanostructures Morphology Measurements, Calculations, And Model Fittings. We carried out five identical SPERISE experiments under the same condition for three different crystalline substrates each time, and varied the processing time from 30 s to 5 min with a 30 s time interval. Immediately after processing, the substrates were examined in SEM for the cross section nanostructure measurements. For nanostructures fabricated in 30 s, the measurements were confirmed with AFM. All data points in Figure 3 were an average of the measurements in the five identical SPERISE experiments.

The height of nanostructures before (H_1 as shown by Figure 3d solid lines) and after (H_2 as shown by Figure 3d dashed lines) oxide removal, the diameter of nanohemispheres (W_1 as shown by Figure 3e), the base diameter (W_2 as shown by Figure 3h) are the direct measurements. The total height reduction (H_3 as shown by Figure 3d dash−dot lines) is calculated by $H_1 - H_2$. The height of original etched nanocones (H_4 as shown by Figure 3f dash lines) is calculated by $H_1 - {}^1/_2W_1$. The height reduction caused by inward oxidation (H_5 as shown by Figure 3g) is calculated by $H_4 - H_2$. The aspect ratio (Figure 3i) is calculated by H_2/W_2.

Diameter of nanohemispheres W_1 is fitted with power function.[18−20] The height of original etched nanocones H_4 and nanocone base diameter W_2 are linearly fitted as it represents the result of etching process. The inward oxidation thickness H_5 is fitted with quadratic function.[21] The aspect ratio is fitted with a constant. The height of nanostructures before (H_1) and after (H_2) oxide removal are fitted with models $H_4 + W_1$ and $H_4 - H_5$, respectively.

Several other models were tried, such as fitting H_1 and H_2 with a linear model, and fitting W_1 with quadratic function, and the models adopted here represented the best fitting results with minimum error. This additional evidence validates our proposed mechanisms.

Optical Absorption Measurements. To quantitatively characterize the optical absorption of the silicon nanocone array substrates, reflection and transmission spectroscopy measurements were carried out, respectively. The normalized optical absorption is calculated by subtracting the sum of normalized reflection and transmission from unity. The total reflection and transmission from all angles were measured at the wavelengths ranging from 300 to 1000 nm. The optical reflectance at all angles in the hemispherical space was measured by Varian Cary 5G UV−vis−NIR spectrophotometer with a Cary integrating sphere attachment. A reflectance standard sample (reflectance exceeding 99% from 400−1500 nm) was used to calibrate the system first, and the reflectance of the samples were measured at the wavelengths ranging from 300 to 1000 nm (the most reliable range of the equipment). The transmission in the same wavelength was measured by a standard setup of the system. This setup is only able to carry out the measurement with the normal incident angle.

Light Incidence Angle Characterization. An integrating sphere with a center mount sample holder stage (Labsphere RTC-060-SF) was used to characterize the relationship of absorption to angle of incidence (AOI). In our setup, the illumination was provided by a tungsten halogen light source. The beam was collimated and entered into the sphere through a small aperture. The light was simultaneously collected by an Ocean Optics broad band spectrometer (450−1000 nm) through the detector port of the sphere. The substrates were fixed by a center mount clip style sample holder, which can change the angle from 0°−90° with the resolution of 1°.

Acknowledgment. This work is partially supported by Illinois ECE startup Grant and NSF Grant ECCS 10-28568. The authors also thank Vania Petrova and Wacek Swiech in the Center for Microanalysis of Materials at the University of Illinois at Urbana−Champaign for the advices and assistance in SEM and TEM imaging.

Supporting Information Available: Supplementary figures and methods and described in the text. This material is available free of charge *via* the Internet at http://pubs.acs.org.

REFERENCES AND NOTES

1. Tsakalakos, L.; Balch, J.; Fronheiser, J.; Korevaar, B. A.; Sulima, O.; Rand, J. Silicon Nanowire Solar Cells. *Appl. Phys. Lett.* **2007**, *91*, 233117–233113.
2. Fan, Z.; Razavi, H; Do, J.-W.; Moriwaki, A.; Ergen, O.; Chueh, Y.-L.; Leu, P. W.; Ho, J. C.; Takahashi, T.; Reichertz, L. A.; *et al.* Three-Dimensional Nanopillar-Array Photovoltaics on Low-Cost and Flexible Substrates. *Nat. Mater.* **2009**, *8*, 648–653.
3. Zhu, J.; Yu, Z.; Burkard, G. F.; Hsu, C.-M.; Connor, S. T.; Xu, Y.; Wang, Q.; McGehee, M.; Fan, S.; Cui, Y. Optical Absorption Enhancement in Amorphous Silicon Nanowire and Nanocone Arrays. *Nano Lett.* **2008**, *9*, 279–282.
4. Sears, G. W. A Growth Mechanism for Mercury Whiskers. *Acta Metall.* **1955**, *3*, 361–366.
5. Wagner, R. S.; Ellis, W. C. Vapor−Liquid−Solid Mechanism of Single Crystal Growth. *Appl. Phys. Lett.* **1964**, *4*, 89–90.
6. Yan, H. F.; Xing, Y. J.; Hang, Q. L.; Yu, D. P.; Wang, Y. P.; Xu, J.; Xi, Z. H.; Feng, S. Q. Growth of Amorphous Silicon Nanowires *via* a Solid−Liquid−Solid Mechanism. *Chem. Phys. Lett.* **2000**, *323*, 224–228.
7. Mårtensson, T.; Carlberg, P.; Borgström, M.; Montelius, L.; Seifert, W.; Samuelson, L. Nanowire Arrays Defined by Nanoimprint Lithography. *Nano Lett.* **2004**, *4*, 699–702.
8. Shir, D.; Yoon, J.; Chanda, D.; Ryu, J.-H.; Rogers, J. A. Performance of Ultrathin Silicon Solar Microcells with Nanostructures of Relief Formed by Soft Imprint Lithography for Broad Band Absorption Enhancement. *Nano Lett.* **2010**, *10*, 3041–3046.
9. Park, M.; Harrison, C.; Chaikin, P. M.; Register, R. A.; Adamson, D. H. Block Copolymer Lithography: Periodic Arrays of $\sim 10^{11}$ Holes in 1 Square Centimeter. *Science* **1997**, *276*, 1401–1404.
10. Huang, Z.; Zhang, X; Reiche, M.; Liu, L.; Lee, W.; Shimitzu, T.; Senz, S.; Gosele, U. Extended Arrays of Vertically Aligned Sub-10 nm Diameter [100] Si Nanowires by Metal-Assisted Chemical Etching. *Nano Lett.* **2008**, *8*, 3046–3051.
11. Levchenko, I.; Cvelbar, U.; Ostrikov, K. Kinetics of the Initial Stage of Silicon Surface Oxidation: Deal—Grove or Surface Nucleation? *Appl. Phys. Lett.* **2009**, *95*, 021502–021503.
12. Jansen, H.; de Boer, M.; Legtenberg, R.; Elwenspoek, M. The Black Silicon Method: A Universal Method for Determining the Parameter Setting of a Fluorine-Based Reactive Ion Etcher in Deep Silicon Trench Etching with Profile Control. *J. Micromech. and Microeng.* **1995**, *5*, 115.
13. Clemm, P. J.; Fisher, J. C. The Influence of Grain Boundaries on the Nucleation of Secondary Phases. *Acta Metall.* **1995**, *3*, 70–73.

14. Deal, B. E.; Grove, A. S. General Relationship for the Thermal Oxidation of Silicon. *J. Appl. Phys.* **1965**, *36*, 3770–3778.
15. Emerson, W. Electromagnetic Wave Absorbers and Anechoic Chambers through the Years. *IEEE Trans. Antennas Propogation* **1973**, *21*, 484–490.
16. Huang, Y.-F.; Chattopadhyay, Surojit; Jen, Y.-J.; Peng, C.-Y.; Liu, T.-A.; Hsu, Y.-K.; Pan, C.-L.; Lo, H.-C.; Hsu, C.-H.; Chang, Y.-H.; *et al*. Improved Broadband and Quasi-omnidirectional Anti-reflection Properties with Biomimetic Silicon Nanostructures. *Nat. Nanotechnol.* **2007**, *2*, 770–774.
17. Kelzenberg, M. D.; Boettcher, S. W.; Petykiewicz, J. A.; Turner-Evans, D. B.; Putman, M. C.; Warren, E. L.; Spurgeon, J. M.; Briggs, R. M.; Lewis, N. S.; Atwater, H. A. Enhanced Absorption and Carrier Collection in Si Wire Arrays for Photovoltaic Applications. *Nat. Mater.* **2010**, *9*, 239–244.
18. Turnbull, D.; Fisher, J. C. Rate of Nucleation in Condensed Systems. *J. Chem. Phys.* **1949**, *17*, 71–73.
19. Zener, C. Theory of Growth of Spherical Precipitates from Solid Solution. *J. Appl. Phys.* **1949**, *20*, 950–953.
20. Laaksonen, A.; Talanquer, V.; Oxtoby, D. W. Nucleation: Measurements, Theory, and Atmospheric Applications. *Annu. Rev. Phys. Chem.* **1995**, *46*, 489–524.
21. Deal, B. E.; Grove, A. S. General Relationship for the Thermal Oxidation of Silicon. *J. Appl. Phys.* **1965**, *36*, 3770–3778.